

Parametrically driven pure-Kerr temporal solitons in a chip-integrated microcavity

Received: 27 November 2023

Accepted: 5 February 2024

Published online: 14 March 2024

 Check for updates

Grégory Moille^{1,2}, Miriam Leonhardt^{3,4}, David Paligora^{3,4},
Nicolas Englebert⁵, François Leo⁵, Julien Fatome⁶, Kartik Srinivasan^{1,2} &
Miro Erkintalo^{3,4}✉

The discovery that externally driven nonlinear optical resonators can sustain ultrashort pulses (solitons) corresponding to coherent optical frequency combs has enabled landmark advances in applications from telecommunications to sensing. Most previous research has focused on resonators with purely cubic (Kerr-type) nonlinearity that are externally driven with a monochromatic continuous-wave laser—in such systems, the solitons manifest themselves as unique attractors whose carrier frequency coincides with that of the external driving field. Recent experiments have, however, shown that a qualitatively different type of temporal soliton can arise via parametric downconversion in resonators with simultaneous quadratic and cubic nonlinearity. In contrast to conventional solitons in pure-Kerr resonators, these parametrically driven solitons come in two different flavours with opposite phases, and they are spectrally centred at half of the frequency of the driving field. Here we theoretically predict and experimentally demonstrate that parametrically driven solitons can also arise in resonators with pure-Kerr nonlinearity under conditions of bichromatic driving. In this case, the solitons arise through four-wave-mixing-mediated phase-sensitive amplification, come with two distinct phases and have a carrier frequency in between the two external driving fields. Our experiments are performed in an integrated silicon nitride microcavity, and we observe frequency comb spectra in remarkable agreement with theoretical predictions. In addition to representing the discovery of a new type of temporal dissipative soliton, our results constitute an unequivocal realization of parametrically driven soliton frequency combs in a microcavity platform that is compatible with foundry-ready mass fabrication.

The injection of monochromatic continuous-wave (CW) laser light into dispersive optical resonators with purely Kerr-type $\chi^{(3)}$ nonlinearity can lead to the generation of localized structures known as dissipative Kerr cavity solitons (CSs)^{1,2}. These CSs correspond to ultrashort

pulses of light that can persist in the resonator (Fig. 1a), indefinitely maintaining constant shape and energy³. Since first observed in macroscopic optical fibre ring resonators¹, CSs have attracted particular attention in the context of monolithic Kerr microcavities², where they

¹Joint Quantum Institute, NIST/University of Maryland, College Park, MD, USA. ²Microsystems and Nanotechnology Division, National Institute of Standards and Technology, Gaithersburg, MD, USA. ³Department of Physics, University of Auckland, Auckland, New Zealand. ⁴The Dodd-Walls Centre for Photonic and Quantum Technologies, Dunedin, New Zealand. ⁵Service OPERA-Photonique, Université libre de Bruxelles (U.L.B.), Brussels, Belgium. ⁶Laboratoire Interdisciplinaire Carnot de Bourgogne, UMR 6303 CNRS Université de Bourgogne, Dijon, France. ✉e-mail: m.erkintalo@auckland.ac.nz

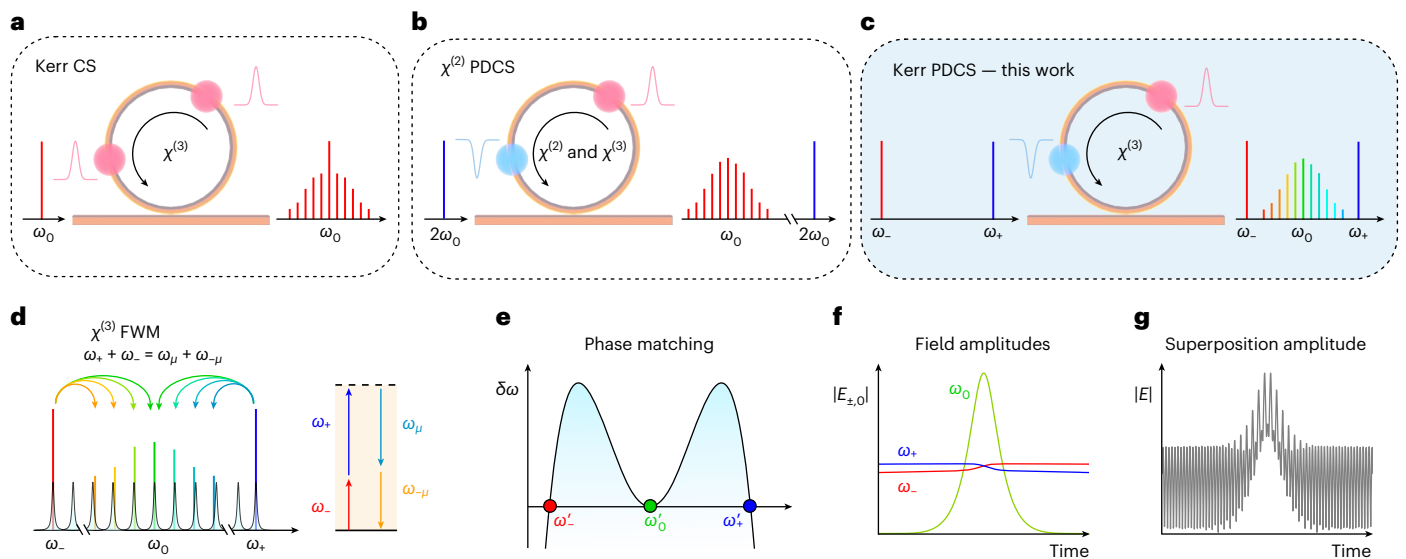


Fig. 1 | Comparison of platforms and schematic illustration of parametrically driven cavity soliton (PDCS) generation in Kerr resonators. a, Conventional Kerr CSs^{1,2,4} form around the input frequency ω_0 in dispersive resonators with $\chi^{(3)}$ Kerr nonlinearity; for given parameters, all solitons in the resonator are identical. **b**, Parametric downconversion of an input field at $2\omega_0$ can yield PDCSs at ω_0 in a resonator with combined $\chi^{(2)}$ and $\chi^{(3)}$ nonlinearity^{26,27}. Here, the solitons come in two forms with opposite phase²⁶: the complex soliton electric field $E_{\pm}(\tau) \propto \pm E_0(\tau) \exp(i\omega_0\tau)$, where $\pm E_0(\tau)$ is the slowly varying envelope (the real part visualized in **a–c**) and i is the imaginary unit. **c**, The bichromatically driven Kerr resonator configuration studied in this work, where PDCSs arise in between two input frequencies ω_{\pm} . **d**, Schematic of the non-degenerate FWM process (and the corresponding energy flow diagram) through which the intracavity fields at ω_{\pm} provide coherent parametric driving to all of the PDCS comb lines around ω_0 .

Note that this energy flow is in contrast to the standard Kerr CS case in **a**, where only the mode ω_0 is driven. The shaded curves in the background of the schematic depict cavity modes. **e**, PDCSs arise under conditions close to linear phase matching of degenerate FWM, which in terms of cavity modes occurs when the frequency deviation $\delta\omega = (\omega'_+ + \omega'_-)/2 - \omega'_0 \approx 0$, with ω'_{\pm} being the driven cavity modes and ω'_0 the mode closest to ω_0 . **f**, Schematic of the slowly varying electric field amplitudes around the parametric signal frequency ω_0 (E_0 , green) and the pump frequencies ω_{\pm} (E_{\pm} , blue and red). The fields E_{\pm} must be approximately CW to ensure a homogeneous parametric driving strength, calling for (1) sufficient dispersive walk-off to mitigate pump depletion and (2) suppression of modulation instabilities. **g**, Because the full intracavity field consists of a superposition of the E_{\pm} and E_0 components, the PDCS manifests itself as a localized structure amidst a rapidly oscillating background.

underpin the generation of coherent and broadband optical frequency combs^{4–6}. By offering a route to coherent frequency comb generation in chip-integrated, foundry-ready platforms, CSs have enabled groundbreaking advances in applications including telecommunications^{7,8}, artificial intelligence^{9,10}, astronomy^{11,12}, frequency synthesis¹³, microwave generation^{14,15} and distance measurements^{16,17}.

The conventional CSs that manifest themselves in resonators with pure-Kerr nonlinearity sit atop a CW background, and they gain their energy through four-wave mixing (FWM) interactions with that background¹. In the frequency domain, the solitons are (to first order) centred around ω_0 , the frequency of the external CW laser that drives the resonator (Fig. 1a). They are (barring some special exceptions^{18–21}) unique attracting states: except for trivial time translations, all of the CSs that exist for given system parameters are identical. These features can be disadvantageous or altogether prohibitive for selected applications: noise on the external CW laser can degrade the coherence of nearby comb lines, and removal of the CW background may require careful spectral filtering to avoid the saturation of amplifiers or detectors (a drop-port can mitigate this issue but comes with additional losses), whereas applications that require the coexistence of distinguishable binary elements^{22–25} are fundamentally beyond reach. Interestingly, recent experiments have revealed that qualitatively different types of CS can exist in resonators that display a quadratic $\chi^{(2)}$ in addition to a cubic $\chi^{(3)}$ nonlinearity (Fig. 1b); in particular, degenerate optical parametric oscillators driven at $2\omega_0$ can support CSs at ω_0 (refs. 26,27). In this configuration, the solitons are parametrically driven through the quadratic downconversion of the externally injected field, which endows them with fundamental differences compared with the conventional CSs emerging in monochromatically driven, pure-Kerr resonators. Specifically, parametrically driven cavity solitons (PDCSs)

are spectrally separated from the driving frequency (for example, ω_0 versus $2\omega_0$), and they come in two binary forms with opposite phase. These traits render PDCSs of interest for an altogether new range of applications.

Optical PDCSs have so far been generated only via the quadratic $\chi^{(2)}$ nonlinearity, which is not yet intrinsically available in integrated (foundry-ready) resonator platforms, such as silicon²⁸ or silicon nitride^{29–31}. However, it is well known that phase-sensitive amplification analogous to $\chi^{(2)}$ parametric downconversion can also be realized in pure-Kerr resonators when driven using two lasers with different carrier frequencies^{32–35}, enabling, for example, novel random number generators^{22,23} and coherent optical Ising machines^{24,25}. While this analogy may allude to the possibility of generating PDCSs in foundry-ready, pure-Kerr resonators with bichromatic driving³⁶, fundamental differences between dispersive $\chi^{(2)}$ and $\chi^{(3)}$ parametric oscillators (for example, the number of potentially resonant fields, the frequency spacing of interacting waves, dispersive phase matching and spurious non-degenerate FWM interactions) prohibit a priori conclusions. The impact of bichromatic driving in the dynamics of conventional Kerr CSs has been considered^{37–41}, but the possibility of using the scheme to generate temporal PDCSs remains entirely unexplored.

Here we theoretically predict and experimentally demonstrate that a dispersive resonator with pure-Kerr nonlinearity can support PDCSs in the presence of bichromatic driving (Fig. 1c). We reveal that, under appropriate conditions, a signal field with a carrier frequency in between two spectrally separated driving fields obeys the damped, parametrically driven nonlinear Schrödinger equation (PDNLSE) that admits PDCS solutions, and we unveil the system requirements for the practical excitation of such solutions. Our experiments are performed using a 23- μm -radius, chip-integrated silicon nitride microring

resonator whose dispersion enables PDCS generation at 253 THz (1,185 nm) when bichromatically pumped at 314 THz (955 nm) and 192 THz (1,560 nm). We observe PDCS frequency comb spectra that are in good agreement with numerical simulations, as well as clear signatures of the anticipated \mathbb{Z}_2 symmetry, that is, the coexistence of two PDCSs with opposite phase. By revealing a new pathway for the generation of coherent PDCS frequency combs far from any pump frequency, in a platform that has direct compatibility with foundry-ready fabrication, our work paves the way for integrated, low-noise frequency comb generation in new spectral regions, as well as the photonic integration of applications requiring combs with a binary degree of freedom.

Results

We first summarize the main points that lead to the prediction of PDCSs in bichromatically driven Kerr resonators (see Methods for full details). To this end, we consider a resonator made from a dispersive, $\chi^{(3)}$ nonlinear waveguide that is driven with two coherent CW fields with angular frequencies ω_{\pm} (see Fig. 1c). The dispersion of the resonator is described by the integrated dispersion (D_{int})⁶ at the cavity resonance ω'_0 (primes highlight resonance frequencies throughout the article) closest to the frequency $\omega_0 = (\omega_+ + \omega_-)/2$:

$$D_{\text{int}}(\mu) = \omega'_\mu - \omega'_0 - \mu D_1 = \sum_{k \geq 2} \frac{D_k}{k!} \mu^k. \quad (1)$$

Here, μ is a relative mode number with respect to the resonance ω'_0 and $D_1/(2\pi)$ is the cavity free-spectral range (FSR) at ω'_0 . The terms D_k with $k > 1$ account for deviations of the resonance frequencies ω'_μ from an equidistant grid defined by $\omega'_0 + \mu D_1$.

Under particular conditions (see Methods), the evolution of the slowly varying electric field envelope centred at ω_0 can be shown to be (approximately) governed by the PDLSE, with the parametric driving ensuing from non-degenerate FWM driven by the intracavity fields at the pump frequencies ($\omega_+ + \omega_- \rightarrow \omega_\mu + \omega_{-\mu}$; Fig. 1d). (Note that in stark contrast to standard Kerr CSs, for which only one comb line is externally driven, all of the components of a PDCS frequency comb are separately driven via non-degenerate FWM.) Because the PDLSE is well known to admit PDCS solutions^{26,42}, it follows that the system may support such solitons with a carrier frequency ω_0 in between the two driving frequencies, provided, however, that the system parameters—particularly the resonator dispersion—are conducive for soliton existence.

The resonator dispersion must meet three key conditions for PDCS excitation to be viable (Methods). First, for solitons to exist, the dispersion around the degenerate FWM frequency ω_0 must be anomalous, that is, $D_2 > 0$ in equation (1). Second, the effective detuning (see Methods) between the degenerate FWM frequency (ω_0) and the closest cavity resonance (ω'_0) must be within the range of soliton existence, essentially requiring that the degenerate FWM process $\omega_+ + \omega_- \rightarrow 2\omega_0$ (approximately) satisfies linear phase matching (Fig. 1e). This second condition can be written as $\delta\omega = (\omega'_+ + \omega'_-)/2 - \omega'_0 = [D_{\text{int}}(p) + D_{\text{int}}(-p)]/2 \approx 0$, where $\pm p$ corresponds to the modes excited by the driving lasers at ω_{\pm} . Given that $D_2 > 0$, this requires at least one higher-even-order coefficient (for example, D_4) to be negative. Third, the intracavity field amplitudes at the driving frequencies, $|E_{\pm}|$, must remain (approximately) homogeneous and stationary to ensure a constant parametric driving strength for the PDCS field E_0 centred at ω_0 (Fig. 1f). This final condition can be met by ensuring that the dispersion at the driving frequencies is (1) normal (or driving amplitudes small), such that the corresponding intracavity fields do not undergo pattern forming (modulation) instabilities⁴³ and (2) such that the temporal walk-off between the driving frequencies ω_{\pm} and the signal frequency ω_0 is sufficiently large so as to mitigate pump depletion in the vicinity of the soliton that would otherwise break the homogeneity of the fields at ω_{\pm} (Fig. 1f). As will be demonstrated below, all of these conditions can be met through

judicious dispersion engineering that is well within the reach of contemporary photonic integrated circuit fabrication.

Simulations

Before discussing our experiments, we present results from numerical simulations that illustrate the salient physics. Our simulations are based on a full iterative ‘keda’ map of the system without any approximations (Methods), and they consider a toy resonator with 25 GHz FSR and minimal dispersion that is necessary for PDCS existence (see Fig. 2a). Specifically, we assume a quartic dispersion with $D_2 = 2\pi \times 4.1$ kHz and $D_4 = -2\pi \times 33$ mHz, yielding $D_{\text{int}}(p) + D_{\text{int}}(-p) \approx 0$ for a pump frequency shift $\Omega_p = 2\pi \times 30.4$ THz (corresponding to relative mode number $\mu_{\pm} = \pm p = \pm 1,217$). We assume for simplicity that the two driving fields are coincident on their respective linear cavity resonances (zero detuning) and both carry a CW laser power of about 140 mW (see Methods for other parameters). Because the group-velocity dispersion at the pump frequencies is normal, modulational instabilities are suppressed and the intracavity fields converge to stable homogeneous states with an equal circulating CW power of about 43 W, thus yielding an effective parametric driving strength and detuning within the regime of PDCS existence (see Methods). Figure 2b shows the evolution of the numerically simulated intracavity intensity profile with an initial condition consisting of two hyperbolic secant pulses with opposite phases. As can be seen, after a short transient, the field reaches a steady state that is indicative of two pulses circulating around the resonator. The pulses sit atop a rapidly oscillating background that is due to the beating between the quasi-homogeneous fields at the pump frequencies (Fig. 2c). Correspondingly, the spectrum of the simulation output (Fig. 2d) shows clearly the presence of a hyperbolic secant-shaped feature that sits in between the strong quasi-monochromatic components at the pump frequencies, with a spectral width similar to the bandwidth of parametric gain provided by the pump fields (see Supplementary Note 1). In accordance with PDCS theory (see Methods), there is no notable CW peak at the parametric signal frequency ω_0 at which the solitons are spectrally centred. To highlight the phase disparity of the steady-state pulses, we apply a numerical filter to remove the quasi-monochromatic intracavity components around the pump frequencies and plot in Fig. 2e the real part (Re) of the complex intracavity electric field envelope. The simulation results in Fig. 2e are compared against the real parts of the exact, analytical PDCS solutions (Methods), and we clearly observe excellent agreement.

The results in Fig. 2a–e corroborate the fundamental viability of our scheme. However, they were obtained assuming a completely symmetric dispersion profile with no odd-order terms, which may be difficult to realize even with state-of-the-art microphotonic fabrication (including the resonators considered in our experiments). We find, however, that PDCSs can exist even in the presence of odd-order dispersion, albeit in a perturbed form. This point is highlighted in Fig. 2f–h, which show results from simulations with all of the parameters as in Fig. 2a–e but with an additional non-zero third-order dispersion term $D_3 = -2\pi \times 58$ Hz. As for conventional (externally driven) Kerr CSs^{5,44}, we find that third-order dispersion causes the solitons to emit dispersive radiation at a spectral position determined by the phase-matching condition $D_{\text{int}}(\mu_{\text{DW}}) \approx (\omega_0 - \omega'_0)$ (Fig. 2g). This emission results in the solitons experiencing constant drift in the temporal domain and endows them with oscillatory tails (Fig. 2h). However, as can clearly be seen, the PDCSs continue to exist in two distinct forms with near-opposite phase. It is worth noting that, for the parameters considered in Fig. 2f–h, the low-frequency driving field experiences anomalous group-velocity dispersion; however, the intracavity intensity at that frequency is below the modulation instability threshold⁴³, thus allowing the corresponding field to remain quasi-homogeneous (the modulation on the total intensity profile arises solely from the linear beating between the different fields).

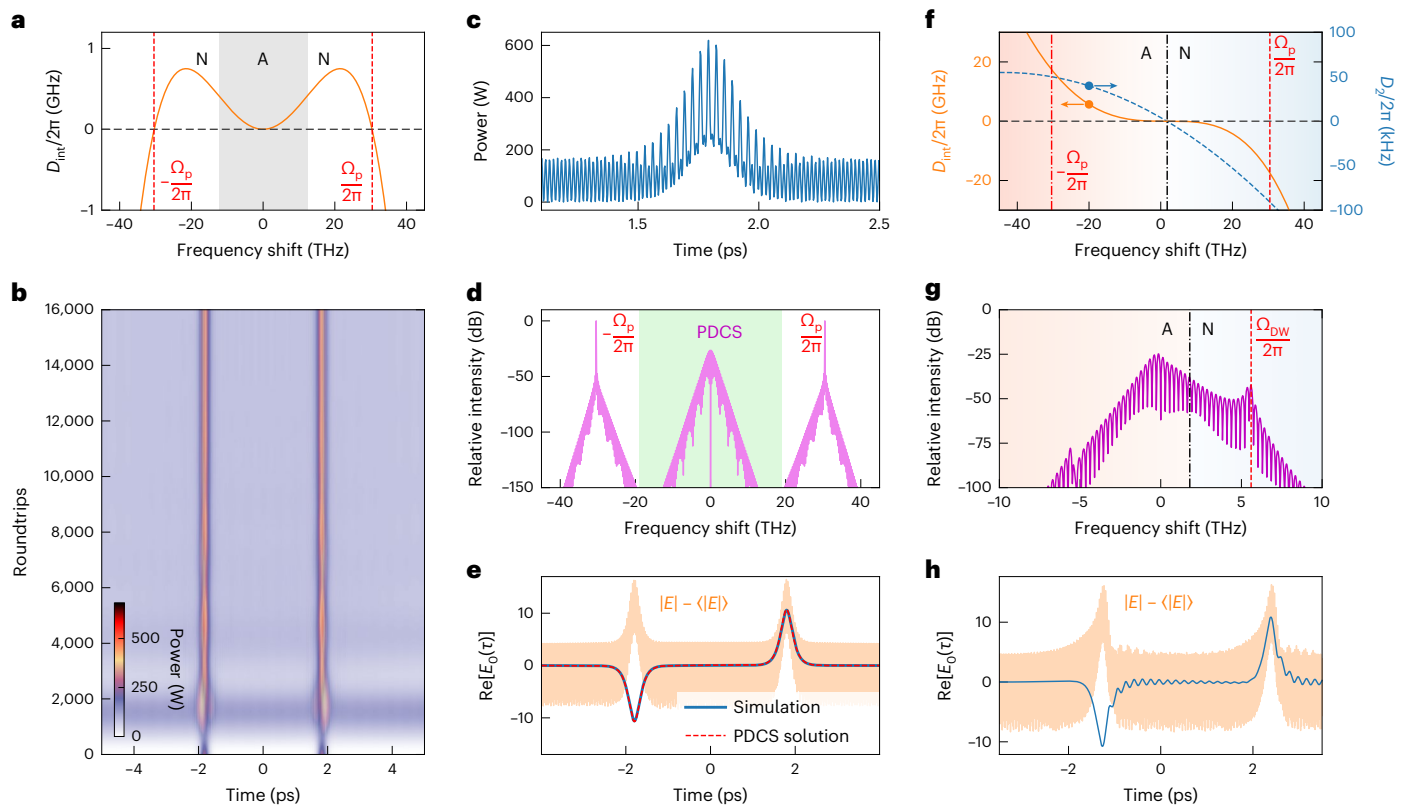


Fig. 2 | Illustrative simulations of PDCS in dispersive Kerr resonators.

a–e. Simulation results obtained for a 25 GHz toy resonator with $D_2 = 2\pi \times 4.1$ kHz and $D_4 = -2\pi \times 33$ mHz. **a**, Integrated dispersion, with the grey shading highlighting a region of anomalous (A) dispersion sandwiched between regions of normal (N) dispersion. Note that, because D_{int} is completely symmetric in this example, the frequency mismatch $\delta\omega(p)$ is equal to $D_{\text{int}}(p)$, such that the pump frequencies satisfying linear phase matching ($\delta\omega = 0$) can be directly read off the graph. The vertical dashed lines indicate those pump frequencies and were used in the simulations. **b**, Dynamical evolution of two hyperbolic secant pulses with opposite phase (see also Supplementary Video 1). The colourmap depicts instantaneous power in watts. **c**, Temporal intensity profile around one of the steady-state solitons at the output of the simulation in **b**; see Extended Data Fig. 1 for an expanded intensity profile. **d**, Optical spectrum corresponding to the output of the simulation in **b**. **e**, The real parts of the analytical PDCS solution (dashed red curve; see Methods) and the simulated intracavity field about zero frequency shift (solid blue curve). The simulation result was obtained by first

spectrally filtering out the intracavity fields at the pump frequencies (green shaded area in **d** indicates the filter passband). The orange curve shows the (mean-subtracted) total field amplitude for reference. **f–h**, Simulation results with the same parameters as in **a–e** but with an additional third-order dispersion term $D_3 = -2\pi \times 58$ Hz. **f**, Integrated dispersion (left axis) and corresponding group-velocity dispersion D_2 (right axis). Note that the frequency mismatch, $\delta\omega(p)$, for this dispersion is identical to the one in **a** (and can thus be read directly from the graph in **a**). **g**, PDCS spectrum in the presence of third-order dispersion. The vertical dashed red line indicates the predicted dispersive wave position. In **f** and **g**, the vertical dash-dotted black line indicates the zero-dispersion point that demarcates regions of normal (N) and anomalous (A) dispersion. **h**, The real part of the simulated intracavity field about zero frequency shift (solid blue curve) and the (mean-subtracted) total field amplitude (orange curve) added for reference (as in **e**) but with third-order dispersion. No analytical solution exists in the presence of third-order dispersion.

Experiments

For experimental demonstration (see Fig. 3a and Methods), we use a microring resonator made from a 690-nm-thick, 850-nm-wide silicon nitride layer embedded in fused silica, fabricated in a commercial foundry. The ring, which exhibits a radius of 23 μm and an FSR of 1 THz, was not specifically designed for this work; it was available to us ‘off the shelf’ because of earlier research on conventional Kerr CSs⁴⁵, highlighting that the dispersion requirements for PDCS generation are not overtly stringent. We use two external cavity diode lasers to drive the resonator: one tunable in the telecommunications C-band (from 186 to 198 THz, that is, from 1,613 to 1,515 nm) and the other tunable from 306 to 330 THz (980 to 910 nm). Both driving fields are optically amplified and combined using a wavelength-division multiplexer before being coupled into the resonator via a pulley scheme that ensures efficient coupling at all of the relevant frequencies⁴⁶. At the output of the resonator, 90% of the signal is routed to an optical spectrum analyser for analysis. The remaining 10% is passed through a bandpass filter to remove spectral components around the driving frequencies, thus enabling the parametrically generated signal field to be isolated for characterization.

The orange curve in Fig. 3b depicts the numerically estimated integrated dispersion of the resonator around a cavity mode at 253 THz, obtained through a combination of finite-element modelling and fitting to our experimental observations (see Methods). These data are consistent with experimentally measured resonance frequencies (blue circles), although we caution that our inability to probe the resonances around 253 THz prevents unequivocal evaluation of the integrated dispersion around that frequency (see Methods for a detailed description of how the measured resonance frequencies are extrapolated to yield the data in Fig. 3b). The estimated dispersion can be seen to be such that the requisite phase matching for generating a PDCS at 253 THz ($\delta\omega \approx 0$) can be satisfied, provided that the pump lasers are configured to drive cavity modes at 314 and 192 THz (Fig. 3c).

In our experiments, we set the on-chip driving power for both driving fields to be about 150 mW and tune the high-frequency pump to the cavity mode at 314 THz. We then adiabatically (much slower than any characteristic timescale of the system) tune the low-frequency pump to the cavity mode at 192 THz (from blue to red), maintaining the high-frequency pump at a fixed frequency. As the low-frequency pump

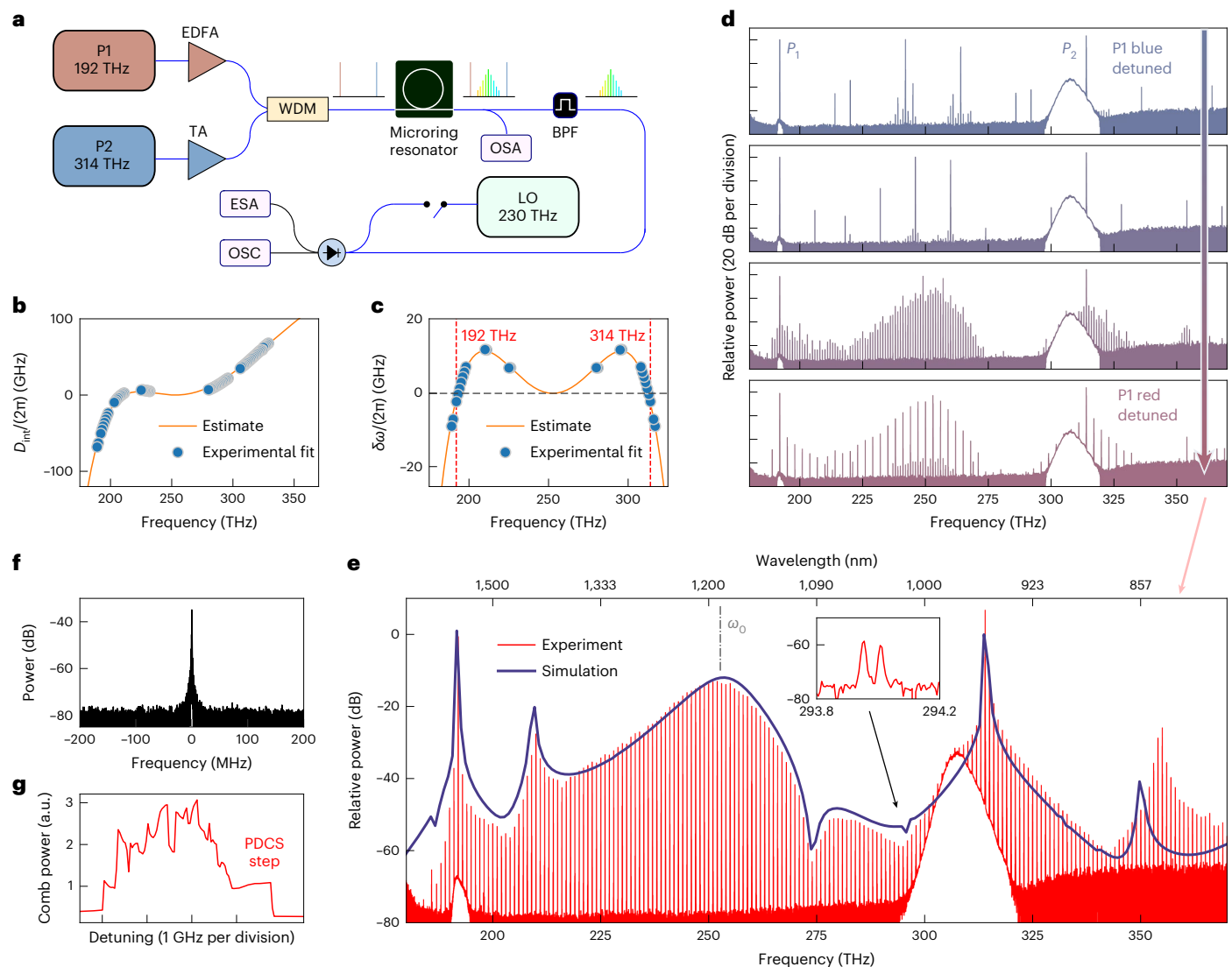


Fig. 3 | Experimental observation of pure-Kerr temporal PDCs in an on-chip microcavity. **a**, Experimental setup. EDFA, erbium-doped fibre amplifier; TA, semiconductor taper amplifier; WDM, wavelength-division multiplexer; OSA, optical spectrum analyser; BPF, bandpass filter; LO, local oscillator; ESA, electrical spectrum analyser; OSC, oscilloscope. **b**, Integrated dispersion around 253 THz used to simulate our experiments (orange curve) and the dispersion fitted from experimental data (blue circles; see Methods). **c**, Linear phase mismatch for the degenerate FWM process computed from the integrated dispersion data in **b**. In **b** and **c**, the fit uncertainties are smaller than the circle markers shown (Methods). **d**, Experimentally measured spectra as the low-frequency pump (P1) tunes into resonance from the blue (the

high-frequency pump P2 is kept fixed). The vertical arrow highlights the redshift of the pump P1. **e**, As the low-frequency pump tunes sufficiently into resonance, the frequency comb spectrum abruptly transitions into a smooth envelope. This transition is indicative of the generation of a single PDCS inside the resonator; the experimentally measured comb spectrum is indeed in good agreement with the numerically simulated spectrum of a single PDCS (blue curve; see Methods). The inset highlights the offset between the PDCS frequency comb and the comb around the P2 pump frequency. **f**, Heterodyne beat note observed in the PDCS regime (the instrument resolution bandwidth is 10 kHz). **g**, Photodetector signal as the low-frequency pump is tuned across a resonance, revealing a step feature that coincides with the emergence of the smooth PDCS comb envelope in **e**.

tunes into resonance, we initially observe non-degenerate parametric oscillation characterized by the generation of two CW components symmetrically detuned about 253 THz. These CW components progressively shift closer to each other as the pump tunes into the resonance, concomitant with the formation of a frequency comb around the degenerate FWM frequency ω_0 (Fig. 3d). To characterize the comb noise, we performed a heterodyne beat measurement using a helper laser at 230 THz in the vicinity of a single comb line. Initially, no beat note is observed, which is characteristic of an unstable, non-solitonic state within the resonator. Remarkably, as the 192 THz driving field is tuned further into resonance, we observe that the parametric signals reach degeneracy, concomitant with the emergence of a broadband comb state with a smooth spectral envelope (Fig. 3e) and a heterodyne

beat note (comparable with the helper laser linewidth of 250 kHz) that is considerably narrower than the 300 MHz microcavity linewidth (Fig. 3f and Supplementary Fig. 1).

The emergence of the smooth comb state (Fig. 3e) is associated with an abrupt drop in the photodetector signal recorded around 253 THz, giving rise to a noticeable step-like feature (Fig. 3g). Similar steps are well-known signatures of conventional CSs in monochromatically driven Kerr resonators⁴. It is also well known from that (conventional CS) context that the abrupt drop in intracavity energy makes it challenging to adiabatically reach the soliton regime due to the concomitant drop in resonator temperature; a powerful method to overcome this challenge is to use a second (auxiliary) laser to effectively stabilize the resonator temperature^{47,48}. We believe that the bichromatic

pumping at the core of our PDCS scheme inherently provides such thermal stabilization, explaining how we are able to adiabatically tune into the step region despite the abrupt drop in comb energy.

As shown in Fig. 3e, the smooth spectral envelope observed in the step region is in very good agreement with the spectrum of a 24 fs (full-width at half-maximum) PDCS derived from numerical modelling that uses estimated experimental parameters (Supplementary Fig. 2). The simulations faithfully reproduce the main features of the experimentally observed spectrum, including a strong dispersive wave peak at about 210 THz. We note that the prominent dip at about 275 THz arises due to the frequency dependence of the pulley coupler⁴⁶, which was taken into account ad hoc in our simulations when estimating the spectrum of the out-coupled PDCS (shown as a blue curve in Fig. 3e; see also Methods and Supplementary Fig. 2). The spectral features around 350 THz originate from nonlinear Bragg-scattering-type FWM, whereby the two pumps at ω_{\pm} spectrally translate a portion of the soliton spectrum to an idler at higher frequencies³⁹; we find that this process is linearly phase matched for soliton spectral components at $\omega_s \approx 2\pi \times 232$ THz, yielding a high-frequency idler at $\omega_i \approx 2\pi \times 354$ THz (see Extended Data Fig. 2).

It is interesting to note that, in addition to the frequency comb around the degenerate FWM frequency at 253 THz, frequency combs arise also around both of the pump frequencies. These combs originate from FWM interactions between the pump fields and the comb lines around 253 THz (see also Supplementary Note 2), in a manner similar to spectral extension^{38–40} and two-dimensional frequency comb⁴⁹ schemes studied in the context of conventional Kerr CSs. The combs around the pump frequencies share the line spacing with the comb around 253 THz, but there is a constant offset between the pump and PDCS combs. In our experiments, this comb offset is directly observable in the optical spectrum (inset of Fig. 3e) and is found to be about 50 ± 2 GHz (where the uncertainty is defined by the resolution of the optical spectrum analyser), which is in good agreement with the value of 49 GHz predicted by our modelling (see Methods). All in all, given the considerable uncertainties in key experimental parameters (particularly dispersion and detunings), we find that the level of agreement between the simulations and experiments is remarkable.

The results shown in Fig. 3 are strongly indicative of PDCS generation in our experiments. Further confirmation is provided by observations of low-noise combs with complex spectral structures that afford a straightforward interpretation in terms of multi-PDCS states (Fig. 4). Specifically, while a single PDCS circulating in the resonator yields a smooth spectral envelope (as in Fig. 3e), the presence of multiple PDCSs results in a spectral interference pattern whose details depend on the soliton's relative temporal delay and—importantly—phase. In our experiments, we can routinely observe comb states indicative of two PDCSs (albeit less frequently than single-soliton states). Figure 4a,b shows selected examples of two-soliton comb spectra measured in our experiments. We draw particular attention to the fact that, in the measured data shown in Fig. 4b, the comb component at the degenerate FWM frequency ω_0 is suppressed (as in Fig. 2d) by about 40 dB compared with neighbouring lines, which is in stark contrast with results in Fig. 4a, in which the degenerate FWM component is dominant. The suppression of the degenerate FWM component in Fig. 4b—together with a narrow heterodyne beat signal and the conspicuous spectral interference features—strongly suggests that the intracavity field consists of two localized structures with near-opposite phase.

The spectral measurements shown in Fig. 4a,b are consistent with the interpretation of two PDCSs with equal (Fig. 4a) or opposite (Fig. 4b) phase. To more quantitatively demonstrate this consistency, we construct theoretical fields consisting of two linearly superposed, temporally delayed PDCSs, with the relative delay ($\Delta\tau$) and phase ($\Delta\phi$) between the solitons inferred by fitting to the experimentally measured spectra (see also Methods). For Fig. 4a, we obtain a best fit with

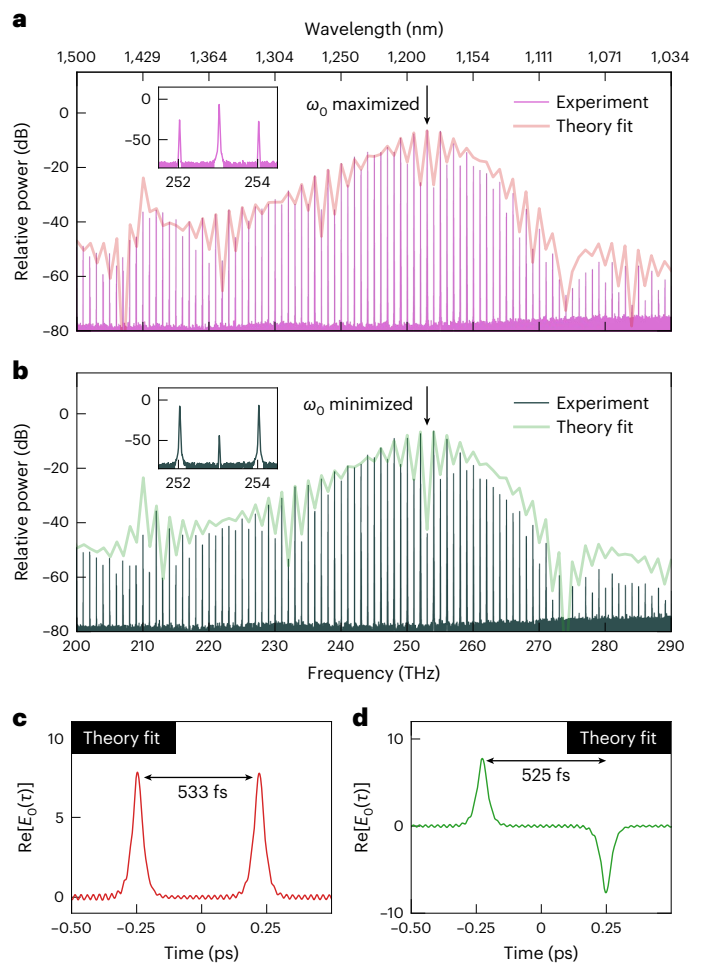


Fig. 4 | Observations of multi-soliton interference. **a–d**, Comb spectra indicative of coherent states with two PDCSs with equal **(a)** or opposite **(b)** phase simultaneously circulating in the resonator. The red and green shaded curves of **a** and **b**, respectively, depict theoretically constructed, out-coupled spectral envelopes of the two-soliton fields, whose real parts are shown in **c** and **d**, respectively. The two-soliton fields were created by linearly superposing two PDCS solutions with different relative delay and phase as inferred from fitting to the experimental spectra (Methods). In **c**, the solitons are in phase and have a relative temporal separation of 533 fs, whereas in **d** the solitons are out of phase (relative phase 0.992π) and have a temporal separation of 525 fs. The insets in **a** and **b** show expanded views of the measured comb spectra around the degenerate FWM frequency 253 THz, highlighting how the degenerate FWM component at 253 THz is maximized **(a)** and minimized **(b)**.

$\Delta\tau = 533$ fs and $\Delta\phi = 0$; for Fig. 4b, we obtain a best fit with $\Delta\tau = 525$ fs and $\Delta\phi = 0.992\pi$.

Figure 4c,d shows the real parts of the theoretically constructed complex field envelopes that yield the best fits to the experimental data, whereas the solid curves in Fig. 4a,b show the corresponding intensity spectra. We see that the theoretically constructed spectra are in good agreement with the experimental observations, supporting the interpretation that the measured comb states are indeed composed of two PDCSs with equal or opposite phase. Unequivocal conclusions would require direct temporal measurements that resolve the intensity and phase of the intracavity waveform²⁶, but such measurements are not possible due to our resonator's very large (1 THz) FSR and the soliton's unconventional 1,200 nm centre wavelength. Nonetheless, the experimental data available (for example, spectral interference profiles, suppression of degenerate FWM component and clean heterodyne beat signal) provide strong support for the proposition that

our bichromatically driven Kerr resonator can support the coexistence of pulses with opposite phase—a clear signature of PDCSs.

Discussion

Our work predicts and demonstrates that, in addition to conventional Kerr CSs, dispersive Kerr resonators can support a new type of dissipative structure—the PDCS—when bichromatically driven under appropriate conditions. The PDCSs observed in our experiments display similar long-term (free-running) stability as conventional CSs generated in similar systems: once generated, the PDCSs can persist virtually indefinitely provided that the system is not actively perturbed (we have tried and succeeded in maintaining the solitons for a period exceeding 24 hours). While the generation of PDCSs may fundamentally place more stringent requirements on the resonator dispersion and pumping, the differences in complexity rapidly erode when considering conventional CSs with specific characteristics or in specific resonators. For example, CSs with broad (octave-spanning) spectra, or strong dispersive wave components at desired frequencies, already require careful dispersion engineering on a par with the requirements for PDCSs (see also Supplementary Note 3); likewise, bichromatic pumping may be needed even in conventional CS experiments to facilitate soliton excitation^{47,48}, to extend and manipulate the spectrum^{38–40} or to phase lock the soliton comb to a known reference⁵⁰.

We envisage that studying the rich nonlinear dynamics^{51,52}, interactions^{53,54} and characteristics (including quantum^{55,56}) of pure-Kerr PDCSs will draw substantial future research interest, echoing the extensive exploration of conventional Kerr CS dynamics over the past decade^{51–56}. Our prediction and observation that PDCSs can emit dispersive waves when perturbed by higher-order dispersion already exemplify the types of explorations enabled by our work.

From a practical vantage, our scheme offers a route to generate PDCS frequency combs in foundry-ready, chip-integrated platforms with characteristics that are different (and potentially advantageous) compared with those associated with conventional Kerr CSs. For example, owing to the nature of the parametric driving, PDCS combs can be generated at spectral regions where pump lasers are not directly available, and if suitably optimized, they can exhibit improved pump-to-soliton conversion efficiencies (see Supplementary Note 3). The lack of a dominating CW component at the PDCS carrier frequency also alleviates the need for careful spectral shaping, and could result in advantages to noise characteristics. In this context, we emphasize that PDCSs are underpinned by phase-sensitive amplification³², which can theoretically offer a subquantum-limited (squeezed) noise figure^{57–59}. Finally, the fact that PDCSs come in two forms with opposite phase can open the doors to a new range of applications that require a binary degree of freedom, including all-optical random number generation and the realization of coherent optical Ising machines. Although the prospect of such applications has been noted previously in the context of $\chi^{(2)}$ PDCSs²⁶, the use of pure-Kerr $\chi^{(3)}$ resonators can potentially offer complementary advantages, such as spectral flexibility, efficiency and compatibility with existing mass-manufacturing capabilities.

Online content

Any methods, additional references, Nature Portfolio reporting summaries, source data, extended data, supplementary information, acknowledgements, peer review information; details of author contributions and competing interests; and statements of data and code availability are available at <https://doi.org/10.1038/s41566-024-01401-6>.

References

- Leo, F. et al. Temporal cavity solitons in one-dimensional Kerr media as bits in an all-optical buffer. *Nat. Photonics* **4**, 471–476 (2010).
- Kippenberg, T. J., Gaeta, A. L., Lipson, M. & Gorodetsky, M. L. Dissipative Kerr solitons in optical microresonators. *Science* **361**, eaan8083 (2018).
- Wabnitz, S. Suppression of interactions in a phase-locked soliton optical memory. *Opt. Lett.* **18**, 601–603 (1993).
- Herr, T. et al. Temporal solitons in optical microresonators. *Nat. Photonics* **8**, 145–152 (2014).
- Brasch, V. et al. Photonic chip-based optical frequency comb using soliton Cherenkov radiation. *Science* **351**, 357–360 (2016).
- Pasquazi, A. et al. Micro-combs: a novel generation of optical sources. *Phys. Rep.* **729**, 1–81 (2018).
- Marin-Palomo, P. et al. Microresonator-based solitons for massively parallel coherent optical communications. *Nature* **546**, 274–279 (2017).
- Corcoran, B. et al. Ultra-dense optical data transmission over standard fibre with a single chip source. *Nat. Commun.* **11**, 2568 (2020).
- Xu, X. et al. 11 TOPS photonic convolutional accelerator for optical neural networks. *Nature* **589**, 44–51 (2021).
- Feldmann, J. et al. Parallel convolutional processing using an integrated photonic tensor core. *Nature* **589**, 52–58 (2021).
- Suh, M.-G. et al. Searching for exoplanets using a microresonator astrocomb. *Nat. Photonics* **13**, 25–30 (2019).
- Obrzud, E. et al. A microphotonic astrocomb. *Nat. Photonics* **13**, 31–35 (2019).
- Spencer, D. T. et al. An optical-frequency synthesizer using integrated photonics. *Nature* **557**, 81–85 (2018).
- Lucas, E. et al. Ultralow-noise photonic microwave synthesis using a soliton microcomb-based transfer oscillator. *Nat. Commun.* **11**, 374 (2020).
- Kwon, D., Jeong, D., Jeon, I., Lee, H. & Kim, J. Ultrastable microwave and soliton-pulse generation from fibre-photonic-stabilized microcombs. *Nat. Commun.* **13**, 381 (2022).
- Suh, M.-G. & Vahala, K. J. Soliton microcomb range measurement. *Science* **359**, 884–887 (2018).
- Riemensberger, J. et al. Massively parallel coherent laser ranging using a soliton microcomb. *Nature* **581**, 164–170 (2020).
- Nielsen, A. U., Garbin, B., Coen, S., Murdoch, S. G. & Erkintalo, M. Coexistence and interactions between nonlinear states with different polarizations in a monochromatically driven passive Kerr resonator. *Phys. Rev. Lett.* **123**, 013902 (2019).
- Hansson, T. & Wabnitz, S. Frequency comb generation beyond the Lugiato–Lefever equation: multi-stability and super cavity solitons. *J. Opt. Soc. Am. B* **32**, 1259–1266 (2015).
- Xu, G. et al. Spontaneous symmetry breaking of dissipative optical solitons in a two-component Kerr resonator. *Nat. Commun.* **12**, 4023 (2021).
- Lucas, E. et al. Spatial multiplexing of soliton microcombs. *Nat. Photonics* **12**, 699–705 (2018).
- Okawachi, Y. et al. Quantum random number generator using a microresonator-based Kerr oscillator. *Opt. Lett.* **41**, 4194–4197 (2016).
- Okawachi, Y. et al. Dynamic control of photon lifetime for quantum random number generation. *Optica* **8**, 1458–1461 (2021).
- Inagaki, T. et al. Large-scale Ising spin network based on degenerate optical parametric oscillators. *Nat. Photonics* **10**, 415–419 (2016).
- Mohseni, N., McMahon, P. L. & Byrnes, T. Ising machines as hardware solvers of combinatorial optimization problems. *Nat. Rev. Phys.* **4**, 363–379 (2022).
- Englebert, N. et al. Parametrically driven Kerr cavity solitons. *Nat. Photonics* **15**, 857–861 (2021).
- Bruch, A. W. et al. Pockels soliton microcomb. *Nat. Photonics* **15**, 21–27 (2021).
- Thomson, D. et al. Roadmap on silicon photonics. *J. Opt.* **18**, 073003 (2016).

29. Liu, J. et al. High-yield, wafer-scale fabrication of ultralow-loss, dispersion-engineered silicon nitride photonic circuits. *Nat. Commun.* **12**, 2236 (2021).
30. Lu, X., Moille, G., Rao, A., Westly, D. A. & Srinivasan, K. Efficient photoinduced second-harmonic generation in silicon nitride photonics. *Nat. Photonics* **15**, 131–136 (2021).
31. Nitiss, E., Hu, J., Stroganov, A. & Brès, C.-S. Optically reconfigurable quasi-phase-matching in silicon nitride microresonators. *Nat. Photonics* **16**, 134–141 (2022).
32. Mecozzi, A., Kath, W. L., Kumar, P. & Goedde, C. G. Long-term storage of a soliton bit stream by use of phase-sensitive amplification. *Opt. Lett.* **19**, 2050–2052 (1994).
33. Radic, S. & McKinstrie, C. J. Two-pump fiber parametric amplifiers. *Opt. Fiber Technol.* **9**, 7–23 (2003).
34. Okawachi, Y. et al. Dual-pumped degenerate Kerr oscillator in a silicon nitride microresonator. *Opt. Lett.* **40**, 5267–5270 (2015).
35. Andrekson, P. A. & Karlsson, M. Fiber-based phase-sensitive optical amplifiers and their applications. *Adv. Opt. Photonics* **12**, 367–428 (2020).
36. de Valcárcel, G. J. & Staliunas, K. Phase-bistable Kerr cavity solitons and patterns. *Phys. Rev. A* **87**, 043802 (2013).
37. Hansson, T. & Wabnitz, S. Bichromatically pumped microresonator frequency combs. *Phys. Rev. A* **90**, 013811 (2014).
38. Zhang, S., Silver, J. M., Bi, T. & Del’Haye, P. Spectral extension and synchronization of microcombs in a single microresonator. *Nat. Commun.* **11**, 6384 (2020).
39. Moille, G. et al. Ultra-broadband Kerr microcomb through soliton spectral translation. *Nat. Commun.* **12**, 7275 (2021).
40. Qureshi, P. C. et al. Soliton linear-wave scattering in a Kerr microresonator. *Commun. Phys.* **5**, 123 (2022).
41. Taheri, H., Matsko, A. B., Maleki, L. & Sacha, K. All-optical dissipative discrete time crystals. *Nat. Commun.* **13**, 848 (2022).
42. Barashenkov, I. V., Bogdan, M. M. & Korobov, V. I. Stability diagram of the phase-locked solitons in the parametrically driven, damped nonlinear Schrödinger equation. *Europhys. Lett.* **15**, 113 (1991).
43. Coen, S. & Erkintalo, M. Universal scaling laws of Kerr frequency combs. *Opt. Lett.* **38**, 1790–1792 (2013).
44. Coen, S., Randle, H. G., Sylvestre, T. & Erkintalo, M. Modeling of octave-spanning Kerr frequency combs using a generalized mean-field Lugiato–Lefever model. *Opt. Lett.* **38**, 37–39 (2013).
45. Yu, S.-P. et al. Tuning Kerr-soliton frequency combs to atomic resonances. *Phys. Rev. Appl.* **11**, 044017 (2019).
46. Moille, G. et al. Broadband resonator–waveguide coupling for efficient extraction of octave-spanning microcombs. *Opt. Lett.* **44**, 4737–4740 (2019).
47. Zhang, S. et al. Sub-milliwatt-level microresonator solitons with extended access range using an auxiliary laser. *Optica* **6**, 206–212 (2019).
48. Zhou, H. et al. Soliton bursts and deterministic dissipative Kerr soliton generation in auxiliary-assisted microcavities. *Light Sci. Appl.* **8**, 50 (2019).
49. Moille, G. et al. Two-dimensional nonlinear mixing between a dissipative Kerr soliton and continuous waves for a higher-dimension frequency comb. Preprint at <https://arxiv.org/abs/2303.10026> (2023).
50. Moille, G. et al. Kerr-induced synchronization of a cavity soliton to an optical reference. *Nature* **624**, 267–274 (2023).
51. Leo, F., Gelens, L., Emplit, P., Haelterman, M. & Coen, S. Dynamics of one-dimensional Kerr cavity solitons. *Opt. Express* **21**, 9180–9191 (2013).
52. Lucas, E., Karpov, M., Guo, H., Gorodetsky, M. L. & Kippenberg, T. J. Breathing dissipative solitons in optical microresonators. *Nat. Commun.* **8**, 736 (2017).
53. Jang, J. K., Erkintalo, M., Murdoch, S. G. & Coen, S. Ultraweak long-range interactions of solitons observed over astronomical distances. *Nat. Photonics* **7**, 657–663 (2013).
54. Cole, D. C., Lamb, E. S., Del’Haye, P., Diddams, S. A. & Papp, S. B. Soliton crystals in Kerr resonators. *Nat. Photonics* **11**, 671–676 (2017).
55. Bao, C. et al. Quantum diffusion of microcavity solitons. *Nat. Phys.* **17**, 462–466 (2021).
56. Guidry, M. A., Lukin, D. M., Yang, K. Y., Trivedi, R. & Vučković, J. Quantum optics of soliton microcombs. *Nat. Photonics* **16**, 52–58 (2022).
57. McKinstrie, C. J. & Radic, S. Phase-sensitive amplification in a fiber. *Opt. Express* **12**, 4973–4979 (2004).
58. Slavík, R. et al. All-optical phase and amplitude regenerator for next-generation telecommunications systems. *Nat. Photonics* **4**, 690–695 (2010).
59. Ye, Z. et al. Overcoming the quantum limit of optical amplification in monolithic waveguides. *Sci. Adv.* **7**, eabi8150 (2021).

Publisher’s note Springer Nature remains neutral with regard to jurisdictional claims in published maps and institutional affiliations.

Springer Nature or its licensor (e.g. a society or other partner) holds exclusive rights to this article under a publishing agreement with the author(s) or other rightsholder(s); author self-archiving of the accepted manuscript version of this article is solely governed by the terms of such publishing agreement and applicable law.

© The Author(s), under exclusive licence to Springer Nature Limited 2024

Methods

Simulation models

We first describe the theoretical models that describe the dynamics of bichromatically driven Kerr resonators and underpin the simulation results in our work. Our starting point is a polychromatic Ikeda-like map, which we will use to derive an extended mean-field Lugiato–Lefever equation that has been used in previous studies^{37–41,60}. To this end, we consider a Kerr resonator made out of a dispersive waveguide (with length L and propagation constant $\beta(\omega)$) that is driven using two coherent fields with angular frequencies ω_{\pm} (see Fig. 1c). The evolution of the electric field envelope (referenced against the degenerate FWM frequency $\omega_0 = (\omega_+ + \omega_-)/2$) during the m th transit around the resonator is governed by the generalized nonlinear Schrödinger equation:

$$\frac{\partial E^{(m)}(z, \tau)}{\partial z} = i\hat{\beta}_S \left(i \frac{\partial}{\partial \tau} \right) E^{(m)} + i\gamma |E^{(m)}|^2 E^{(m)}. \quad (2)$$

Here, z is a coordinate along the waveguide that forms the resonator, τ is time in a reference frame that moves with the group velocity of light at ω_0 , γ is the Kerr nonlinearity coefficient and $\hat{\beta}_S$ is the dispersion operator

$$\hat{\beta}_S \left(i \frac{\partial}{\partial \tau} \right) = \sum_{k \geq 2} \frac{\beta_k}{k!} \left(i \frac{\partial}{\partial \tau} \right)^k, \quad (3)$$

with $\beta_k = d\beta/d\omega|_{\omega_0}$ the Taylor series expansion coefficients of $\beta(\omega)$ around ω_0 . Note that the single electric field envelope $E^{(m)}(z, \tau)$ contains all the frequency components pertinent to the nonlinear interactions, including the fields at the pump frequencies ω_{\pm} and the signal frequency at ω_0 . Note also that the Taylor series expansion coefficients β_k are linked to the resonance frequency expansion coefficients in equation (1) as $D_k \approx -D_1^{k+1} L \beta_k / (2\pi)$ (ref. 6), such that

$$D_{\text{int}}(\mu) \approx -\frac{D_1 L}{2\pi} \hat{\beta}_S(\mu D_1). \quad (4)$$

The Ikeda-like map consists of equation (2) together with a boundary equation that describes the coupling of light into the resonator. Considering bichromatic driving, the boundary equation reads (see also Supplementary Note 4):

$$\begin{aligned} E^{(m+1)}(0, \tau) &= \sqrt{1 - 2\alpha} E^{(m)}(L, \tau) e^{-i\delta_0} \\ &+ \sqrt{\theta_+} E_{\text{in},+} e^{-i\Omega_p \tau + imb_+} \\ &+ \sqrt{\theta_-} E_{\text{in},-} e^{i\Omega_p \tau + imb_-}. \end{aligned} \quad (5)$$

Here, α is half of the fraction of power dissipated by the intracavity field over one roundtrip, $\delta_0 = 2\pi k - \beta(\omega_0)L$ is the linear phase detuning of the reference frequency ω_0 from the closest cavity resonance (with order k), $E_{\text{in},\pm}$ are the complex amplitudes of the driving fields at ω_{\pm} , respectively, $\Omega_p = pD_1$ (with p a positive integer) represents the angular frequency shifts of the pumps from the reference frequency ω_0 , and θ_{\pm} are the power transmission coefficients that describe the coupling of the driving fields into the resonator. The coefficients b_{\pm} enable us to introduce the phase detunings δ_{\pm} that describe the detunings of the pump frequencies from the cavity resonances closest to them (thus accounting for the fact that the frequency shifts $\omega_0 - \omega_{\pm}$ may not be an exact integer multiple of D_1):

$$b_{\pm} = \delta_{\pm} - \delta_0 + \hat{\beta}_S(\pm\Omega_p)L. \quad (6)$$

Note that the phase detunings δ described above are related to the frequency detunings of the corresponding carrier frequency ω from the closest cavity resonance at ω' as $\delta \approx 2\pi(\omega' - \omega)/D_1$.

Before proceeding, we note that, in our specific configuration, only two of the three detuning terms introduced above (δ_0 and δ_{\pm}) are

independent. This is because the degenerate FWM frequency is completely determined by the pump frequencies, namely, $\omega_0 = (\omega_+ + \omega_-)/2$; therefore, the signal detuning δ_0 can be written in terms of the pump detunings δ_{\pm} as (see Supplementary Note 5):

$$\delta_0 = \frac{\delta_+ + \delta_- + L[\hat{\beta}_S(\Omega_p) + \hat{\beta}_S(-\Omega_p)]}{2}. \quad (7)$$

Substituting this expression for δ_0 into equation (6) yields $b_{\pm} = \pm b$, where

$$b = \frac{\delta_+ - \delta_- + L[\hat{\beta}_S(\Omega_p) - \hat{\beta}_S(-\Omega_p)]}{2}. \quad (8)$$

It can be shown (see Supplementary Note 6) that this coefficient describes the offset, Δf , between the frequency combs forming around ω_0 and ω_{\pm} , namely,

$$\Delta f = \frac{|b|D_1}{(2\pi)^2}. \quad (9)$$

PDCS theory

All of the simulations presented in our work use the full Ikeda-like map defined by equations (2) and (5). However, the system's ability to sustain PDCSs can be inferred more readily from the mean-field limit, obtained under the assumption that the intracavity envelope $E^{(m)}(z, \tau)$ evolves slowly over a single roundtrip (that is, the cavity has a high finesse and the linear and nonlinear phase shifts are all small). In this case, the Ikeda-like map described above can be averaged into the generalized Lugiato–Lefever mean-field equation similar to the one used, for example, in refs. 38–41. We write the equation in normalized form as (see Supplementary Note 7):

$$\begin{aligned} \frac{\partial E(t, \tau)}{\partial t} &= \left[-1 + i(|E|^2 - \Delta_0) + i\hat{\beta} \left(i \frac{\partial}{\partial \tau} \right) \right] E \\ &+ S_+ e^{-i\Omega_p \tau + iat} + S_- e^{i\Omega_p \tau - iat}. \end{aligned} \quad (10)$$

Here, t is a slow time variable that describes the evolution of the intracavity field over consecutive roundtrips (and is thus directly related to the index m of the Ikeda-like map), $S_{\pm} = E_{\text{in},\pm} \sqrt{\gamma L \theta_{\pm}} / \alpha^3$ are the normalized strengths of the driving fields, $\Delta_0 = \delta_0 / \alpha$ is the normalized detuning of the signal field, and the normalized dispersion operator $\hat{\beta}$ is defined as in equation (3) but with normalized Taylor series coefficients d_k such that $\beta_k \rightarrow d_k = [2\alpha / (|\beta_2 L|)]^{k/2} \beta_k L / \alpha$. Finally, the coefficient

$$a = \frac{b}{\alpha} = \frac{\Delta_+ - \Delta_- + [\hat{\beta}(\Omega_p) - \hat{\beta}(-\Omega_p)]}{2}, \quad (11)$$

where $\Delta_{\pm} = \delta_{\pm} / \alpha$ are the normalized detunings of the external driving fields. To avoid notational clutter, we use the symbol Ω_p to represent pump frequency shifts both in our dimensional and normalized equations.

We now make the assumption that the intracavity fields E_{\pm} at the pump frequencies are homogeneous and stationary. (Note that this assumption is not used in any of our simulations.) To this end, we substitute the ansatz

$$\begin{aligned} E(t, \tau) &= E_0(t, \tau) \\ &+ E_+ e^{-i\Omega_p \tau + iat} + E_- e^{i\Omega_p \tau - iat} \end{aligned} \quad (12)$$

into equation (10). We then assume further that the (soliton) spectrum around the degenerate FWM frequency (the Fourier transform of $E_0(t, \tau)$) does not exhibit significant overlap with the pump frequencies. This enables us to separate terms that oscillate with different frequencies, yielding the following equation for the signal field:

$$\frac{\partial E_0(t, \tau)}{\partial t} = \left[-1 + i(|E_0|^2 - \Delta_{\text{eff}}) + i\hat{\beta} \left(i \frac{\partial}{\partial \tau} \right) \right] E_0 + 2iE_+ E_- E_0^* \quad (13)$$

where the effective detuning $\Delta_{\text{eff}} = \Delta_0 - 2(Y_+ + Y_-)$, with $Y_{\pm} = |E_{\pm}|^2$ the normalized intensities at the pump frequencies, includes both linear and nonlinear (cross-phase modulation) phase shifts, and the asterisk denotes complex conjugation. Equation (13) has the form of the PDN-LSE⁶¹ with effective detuning Δ_{eff} and the parametric driving coefficient $v = 2iE_+ E_-$. Accordingly, assuming that the resonator group-velocity dispersion is anomalous ($\beta_2 < 0$) and that higher-order dispersion is weak at the signal frequency, the equation admits (parametrically driven) soliton solutions of the form²⁶:

$$E_0(\tau) = \sqrt{2}\zeta \operatorname{sech}(\zeta\tau) e^{i(\phi+\theta)}, \quad (14)$$

where $\cos(2\phi) = 1/|\zeta|$, $\zeta = \sqrt{\Delta_{\text{eff}} + |\zeta| \sin(2\phi)}$ and $\theta = \arg[iE_+ E_-]$. It should be clear from the last term of equation (13) that all of the frequency components of E_0 are parametrically driven. This is particularly evident when expanding the field as a Fourier series, $E_0(t, \tau) = \sum_n c_n(t) e^{-inD_1\tau}$; the equation of motion for each modal amplitude c_n will include a parametric driving term $2iE_+ E_- c_{-n}^*$. It is also worth noting that equation (14) and the accompanying normalization show that the PDCS temporal and spectral characteristics follow similar parameter scaling laws as conventional Kerr CSs (see Supplementary Note 3).

Of course, the viability of sustaining the PDCS solution described by equation (14) in an actual bichromatically driven Kerr resonator system is contingent on the applicability of the assumptions outlined above. As described in the main text, the assumption that the intracavity fields E_{\pm} at the pump frequencies are homogeneous and stationary leads to the requirements of dispersive walk-off and suppression of modulation instabilities. The requirement for phase matching of the degenerate FWM process ensues from the fact that stable PDCS solutions generically exist only if the effective detuning Δ_{eff} is sufficiently small⁶¹. Indeed, recalling equation (7), we have

$$\Delta_{\text{eff}} = \frac{\Delta_+ + \Delta_- + \hat{\beta}(\Omega_p) + \hat{\beta}(-\Omega_p)}{2} - 2(Y_+ + Y_-). \quad (15)$$

Considering typical parameters, Δ_{eff} and $|\zeta| = 2\sqrt{Y_+ Y_-}$ are of the order of unity for stable solitons to exist^{26,61}, whereas the detunings Δ_{\pm} can be assumed to be small to ensure that sufficient intracavity powers Y_{\pm} can be attained without excessive driving powers $X_{\pm} = |S_{\pm}|^2$. This implies, then, that the pump frequency shift Ω_p must satisfy $[\hat{\beta}(\Omega_p) + \hat{\beta}(-\Omega_p)] \approx 0$. Unpeeling the normalization, and converting to the integrated dispersion defined as equation (1) in the main text, shows that this condition is equivalent with the linear phase matching of degenerate FWM: $D_{\text{int}}(p) + D_{\text{int}}(-p) \approx 0$.

Resonator used in experiments

The chip-integrated microring resonator used in our experiments was fabricated in a commercially available foundry service provided by Ligentec (certain commercial products or names are identified to foster understanding, and such identification does not constitute recommendation or endorsement by the National Institute of Standards and Technology, nor is it intended to imply that the products or names identified are necessarily the best available for the purpose); see ref. 29 for a study of the quality of related fabrication. The resonators are made of a 690-nm-thick layer of silicon nitride, grown via low-pressure chemical vapour deposition, that is fully embedded in fused silica. The ring has a width of 850 nm and a radius of 23 μm , thus yielding a roundtrip length $L = 144.5 \mu\text{m}$. Light is coupled into the ring via a 460-nm-wide integrated bus waveguide, with a 32- μm -long pulley coupler ensuring good coupling at all of the different frequencies of interest (ω_0, ω_{\pm}). The resonator has intrinsic and loaded Q factors of 1.5×10^6 and 0.75×10^6 ,

respectively, corresponding to a finesse of $\mathcal{F} \approx 3,000$, a resonance linewidth of $\Delta f_r \approx 300$ MHz and linear propagation losses of about 0.2 dB cm^{-1} . The chip has an input-to-output insertion loss of about 5.6 dB at 980 nm and 8.4 dB at 1,550 nm. To estimate the resonator's nonlinearity, we used finite-element modelling to simulate the electric field distributions at different frequencies of interest. Considering the nonlinear refractive index of $n_2 \approx 3.1 \times 10^{-15} \text{ cm}^2 \text{ W}^{-1}$ for silicon nitride⁶² (and zero for air), we estimate that the Kerr nonlinearity coefficient γ ranges from 1 to $4 \text{ W}^{-1} \text{ m}^{-1}$ across the frequencies of interest. In our simulations, we use a constant value of $1 \text{ W}^{-1} \text{ m}^{-1}$ for simplicity.

Measurement of comb power signal

The photodetector signal shown in Fig. 3g was obtained by first spectrally filtering out components around the pump frequencies so as to isolate the parametrically generated comb. This filtering incurs significant losses, which cannot be optically compensated due to the unavailability of amplifiers around the comb's 1,200 nm centre wavelength. Owing to the small signal level, the trace shown in Fig. 3g was obtained using a 1 ns photodetector with an electronic pre-amplifier that has a bandwidth of 1 MHz. The comparatively low bandwidth of the pre-amplifier effectively acts as a low-pass filter, explaining why the unstable (noisy) states before the soliton step do not show rapid fluctuations.

Resonator dispersion and thermal nonlinearity

The theoretically estimated resonator dispersion (orange curve in Fig. 3b) was obtained in two steps. We first calculated the theoretical resonance frequencies using finite-element modelling, and then slightly modified those data (see Supplementary Fig. 3 for a comparison of the two integrated dispersion curves) to match the PDCS simulations to the experimentally obtained spectra. This second step can be considered as a 'free parameter' that is necessary to obtain a dispersion profile consistent with our experimental observations. Experimentally, we characterized the dispersion at various spectral regions by measuring the resonance frequencies using a set of widely tunable lasers and a high-resolution wavemeter. Unfortunately, the unavailability of a suitable laser around the degenerate FWM frequency (253 THz) prevented us from probing the dispersion directly at that frequency.

Because we are not able to probe the dispersion around 253 THz, it is not possible to unequivocally compare the experimentally measured dispersion with our theoretical estimate. This is because the integrated dispersion D_{int} depends on the precise resonance frequency ω'_0 and the FSR $[D_1/(2\pi)]$ at ω'_0 , which we are unable to probe experimentally. To nonetheless show that our measurements in different spectral regions are consistent with our theoretical estimate, we can use a nonlinear least-squares method to fit our experimental data to the theoretical data and in doing so obtain experimental estimates for ω'_0 and D_1 , which then enable us to compute the integrated dispersion. The blue dots in Fig. 3a were obtained using this procedure. The fitting also provides the one-standard-deviation errors for the parameter estimates, $\Delta\omega'_0$ and ΔD_1 , which then enable us to compute the fitting errors for $\Delta D_{\text{int}}(\mu)$ and $\Delta\delta\omega(\mu)$. We find that the maximum error (across relative mode order μ) in the estimated D_{int} is $\max[\Delta D_{\text{int}}(\mu)/(2\pi)] \approx 0.50$ GHz, yielding $\max[\Delta\delta\omega(\mu)/(2\pi)] \approx 0.35$ GHz. These errors are smaller than the markers used in Fig. 3b,c, which is why error bars are not shown.

Owing to the resonator's small size, it exhibits a strong thermal nonlinearity⁶³. We leverage this effect to achieve self-stabilization, such that the input lasers can remain free-running but still maintain near-constant detunings. In addition, the thermal nonlinearity causes the resonance frequencies to shift over several gigahertz as the pump laser(s) are tuned into resonance (see, for example, Fig. 3f), which we suspect is key to achieving phase-matched operation (and thus PDCS generation). We also note that the thermal nonlinearity may influence the resonator dispersion directly⁶⁴; while this effect is generally weak

(and underexamined), it is possible that it also influences the precise phase-matching conditions, thus playing a role in our experiments. A detailed study on the impact of the thermal nonlinearity on PDCS generation is beyond the scope of our present work.

Simulation parameters

The simulations in Fig. 2 assume a critically coupled ($\alpha = \theta$) resonator with a roundtrip length $L \approx 8.3$ mm, a nonlinearity coefficient $\gamma = 1.2 \text{ W}^{-1} \text{ km}^{-1}$ and a finesse $\mathcal{F} = \pi/\alpha = 5,000$. The driving fields are positioned at an angular frequency shift $\pm\Omega_p = 2\pi \times 30.4$ THz with respect to the degenerate FWM frequency, corresponding to relative mode number $p = 1,217$. The dispersion coefficients are $\beta_2 = -5 \text{ ps}^2 \text{ km}^{-1}$, $\beta_3 = 0.45 \text{ ps}^3 \text{ km}^{-1}$ and $\beta_4 = 1.6 \times 10^{-3} \text{ ps}^4 \text{ km}^{-1}$, corresponding to $D_2/(2\pi) = 4.06$ kHz, $D_3/(2\pi) = -57.90$ Hz and $D_4 = -0.03$ Hz, respectively.

The above parameters yield an effective (normalized) driving strength $|v| = 1.37$ and detuning $\Delta_{\text{eff}} = 1.2$, which are known to be in the regime of soliton existence²⁶. As a matter of fact, the above parameters were found by looking for the driving powers and frequency shifts that yield these particular values for the driving strength and detuning.

The simulations in Figs. 3 and 4 use experimental values quoted in the main text or in the resonator description above, with the addition that the nonlinearity coefficient was set to $\gamma = 1 \text{ W}^{-1} \text{ m}^{-1}$. The pump detunings were chosen such that, in Fig. 3, the effective driving strength $|v| = 1.28$ and $\Delta_{\text{eff}} = 6$, and in Fig. 4, $|v| = 1.15$ and $\Delta_{\text{eff}} = 5$. (We note that the effective detunings were coarsely tuned so as to match the simulations to the experimentally measured spectra.) The values of pump detunings (normalized to the resonance half-width) yielding these effective parameters were $\Delta_+ = \Delta_- = -3.4$ for Fig. 3 and $\Delta_+ = -3.6$ and $\Delta_- = -4.2$ for Fig. 4. We remark that these detunings are not unequivocal in the sense that similar effective parameters can be obtained for several different detuning combinations given incremental changes to the system parameters (for example, dispersion, pump power).

Frequency-dependent coupling

All of the simulations reported in our manuscript have been obtained using the model defined by equations (2) and (5). However, as explained in the main text (see also Supplementary Fig. 2), when comparing against experimentally measured spectra (Figs. 3 and 4), the simulation outputs were post-processed to account for the frequency-dependent coupling, thus providing an estimate for the out-coupled spectrum. This was achieved by multiplying the simulated intracavity spectra with the frequency-dependent coupling coefficient (Supplementary Fig. 2) obtained from rigorous coupled-mode simulations⁴⁶. These coupled-mode simulations assumed the coupler length to be $31.25 \mu\text{m}$, which was found to provide a better agreement with our experiments compared with the design value of $32 \mu\text{m}$. This discrepancy is reasonable in terms of fabrication tolerances given the high sensitivity to the phase mismatch between the ring and waveguide modes and that any small discrepancy in the side-wall angle or waveguide width could cause a smaller effective pulley. However we note that the obtained length is well within the fabrication tolerance of deep-ultraviolet stepper fabrication. Note that the frequency-dependent coupling was not included explicitly in our numerical simulation model for the sake of simplicity.

Multi-soliton states

Because of pump depletion and finite dispersive walk-off, the PDCS carve a depletion region onto the intracavity fields at the pump frequencies (see Fig. 1f and Supplementary Note 2). These depletion regions are the time-domain manifestations of the frequency combs that form around the pump frequencies, and they give rise to long-range soliton interactions. Compounded by the system's periodic boundary conditions, stable multi-soliton states only exist at selected relative delays (or not at all) in our simulations. On the other hand, it is well known (from studies of conventional Kerr CSs) that experimental systems exhibit imperfections (for example, avoided mode crossings) that,

along with oscillatory tails from dispersive waves, force multi-soliton states to manifest themselves only at some prescribed relative delays⁵⁴. Because the PDCS in our simulations exhibit long-range coupling, it is not possible to obtain a simulation of a multi-soliton state with the same relative delays as in our experiments, unless one has access to full details of the experimental system (including dispersion that captures possible avoided mode crossings), which we do not have.

Because of the above, the theoretical PDCS fields in Fig. 4c,d were created from a single steady-state PDCS—obtained via simulations of equations (2) and (5). Specifically, the two-soliton fields were obtained by linearly adding together two replicas of the single steady-state PDCS state, with the relative delay ($\Delta\tau$) and phase ($\Delta\phi$) between the replicas inferred from nonlinear least-squares fitting to the experimentally observed spectral interference pattern. For both in- and out-of-phase states, our fitting algorithm yields two possible configurations ($\Delta\tau$, $\Delta\phi$) that identically minimize the sum of the squared residuals. For the in-phase configuration, these are (533 fs, $1 \times 10^{-3}\pi$) and (467 fs, $3 \times 10^{-4}\pi$), and for the out-of-phase configuration, they are (525 fs, 0.99π) and (475 fs, 1.01π). In Fig. 4c,d, we plot the configurations associated with the larger delay. The one-standard-deviation errors for the fits are all smaller than (0.4 fs, 0.01π).

Data availability

The data that support the plots within this paper and other findings of this study are available from the corresponding authors upon reasonable request.

References

- Taheri, H., Matsko, A. B. & Maleki, L. Optical lattice trap for Kerr solitons. *Eur. Phys. J. D* **71**, 153 (2017).
- Bondila, M., Barashenkov, I. V. & Bogdan, M. M. Topography of attractors of the parametrically driven nonlinear Schrödinger equation. *Physica D* **87**, 314–320 (1995).
- Krücke, C. J., Fülöp, A., Ye, Z., Andrekson, P. A. & Torres-Company, V. Optical bandgap engineering in nonlinear silicon nitride waveguides. *Opt. Express* **25**, 15370–15380 (2017).
- Carmon, T., Yang, L. & Vahala, K. J. Dynamical thermal behavior and thermal self-stability of microcavities. *Opt. Express* **12**, 4742–4750 (2004).
- Moille, G. et al. Integrated buried heaters for efficient spectral control of air-clad microresonator frequency combs. *APL Photonics* **7**, 126104 (2022).

Acknowledgements

M.E. acknowledges financial support from the Marsden Fund of the Royal Society of New Zealand Te Apārangi. G.M. and K.S. acknowledge support from the NIST-on-a-chip programme. J.F. acknowledges the CNRS (IRP WALL-IN project).

Author contributions

G.M. performed all of the experiments and assisted in the interpretation of the results. M.L. and D.P. contributed to the theoretical development of the scheme and performed initial simulations to confirm the fundamental viability of the scheme. N.E. and F.L. provided guidance on parametrically driven soliton theory. J.F. assisted in the interpretation of Kerr cavity physics. K.S. supervised and obtained funding for the experiments. M.E. developed the theory, performed the simulations and wrote the manuscript with input from all authors.

Competing interests

The authors declare no competing interests.

Additional information

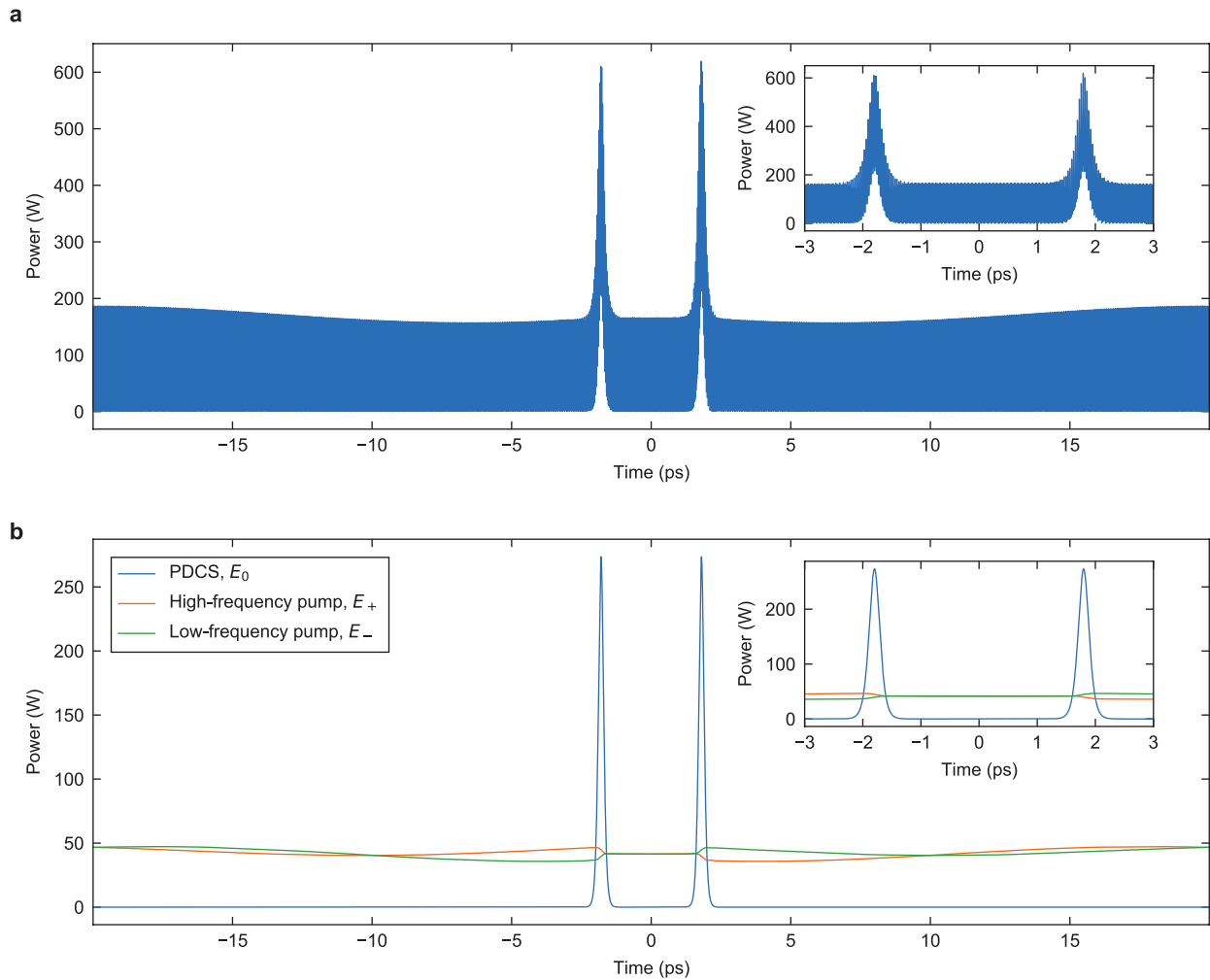
Extended data is available for this paper at <https://doi.org/10.1038/s41566-024-01401-6>.

Supplementary information The online version contains supplementary material available at <https://doi.org/10.1038/s41566-024-01401-6>.

Correspondence and requests for materials should be addressed to Miro Erkintalo.

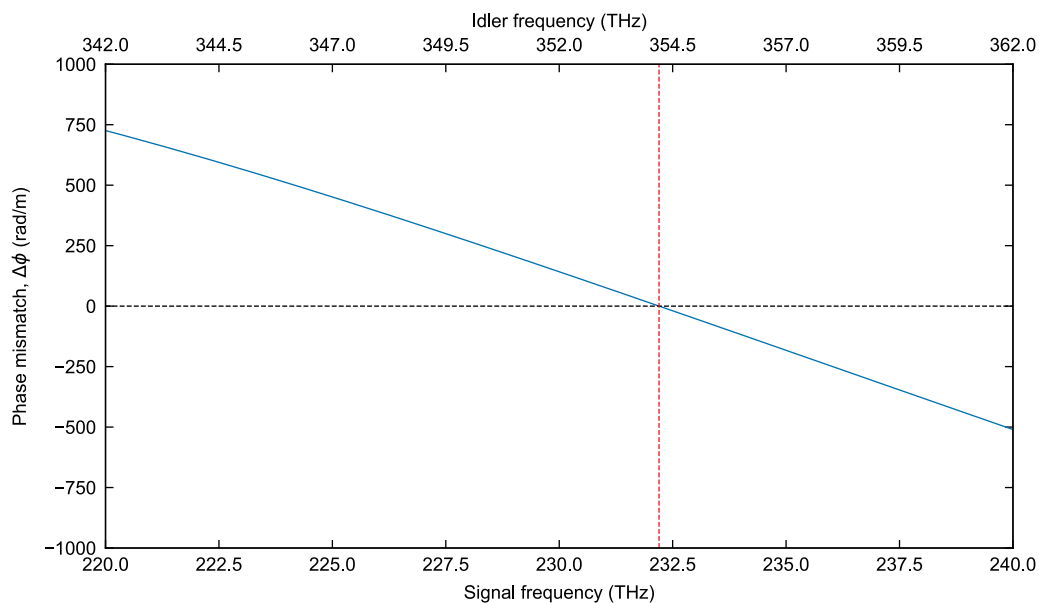
Peer review information *Nature Photonics* thanks Xu Yi and the other, anonymous, reviewer(s) for their contribution to the peer review of this work.

Reprints and permissions information is available at www.nature.com/reprints.



Extended Data Fig. 1 | Extended visualization of numerical simulation results shown in Fig. 2c. (a) Snapshot of the total temporal intensity profile at the simulation output over the entire simulation time window (corresponding to one resonator round trip time). Inset shows a zoom around the two solitons. (b) Temporal intensity profiles of fields centred around the pump frequencies ω_{\pm}

(orange and green curves) and the degenerate FWM frequency $\omega_0 = (\omega_+ + \omega_-)/2$ (blue curve). Inset shows a zoom around the two solitons. The intensity traces in (b) were obtained from the full simulated field envelope by spectrally isolating the relevant frequency components via numerical filtering.



Extended Data Fig. 2 | Linear phase-matching of nonlinear Bragg scattering. Two strong pumps with angular frequencies ω_i (with $\omega_i > \omega_s$) can spectrally translate a low-power signal wave at ω_s to a new idler frequency ω_i via the process of nonlinear Bragg scattering four-wave-mixing: $\omega_i = \omega_s + \omega_p - \omega_p$. The blue solid curve shows the linear phase-mismatch of the Bragg scattering FWM for parameters relevant to our experiment (for example resonator dispersion, pump

frequencies): $\Delta\phi = \beta(\omega_i) + \beta(\omega_p) - \beta(\omega_s) - \beta(\omega_p)$, where $\beta(\omega)$ is the propagation constant of the resonator mode. The phase-mismatch crosses zero at a signal frequency of about 232.5 THz, corresponding to an idler frequency of about 354.5 THz. This phase-matching suggests that the spectral features around 350 THz observed in the experimentally measured spectrum shown in Fig. 3(e) originate from Bragg scattering translation of soliton components at about 232 THz.